SUPPLEMENTAL MATERIAL

The data and code used for the analysis presented in this paper can be accessed at https://github.com/simeonreusch/at2019fdr [1]. `nuztf`, the multimessenger-pipeline used to identify AT2019fdr as potential source, can be found here: https://github.com/desy-multimessenger/nuztf. Both make use of `AMPEL` [2] and `ztfquery` [3].

Follow-up of IC200530A   The high-energy neutrino IC200530A was the tenth alert followed up with our ZTF neutrino follow-up program. It had an estimated 59% probability of being of astrophysical origin, based solely on the reconstructed energy of 82.2 TeV and its zenith angle [4], with a best-fit position of RA[J2000] = $255.37^{+2.48}_{-2.57}$ and Dec[J2000] = $+26.61^{+2.33}_{-2.57}$ at 90% confidence level. The reported localization amounts to a projected rectangular uncertainty area of $25.38\,\mathrm{deg}^2$. During ZTF follow-up observations, 87% of that area was observed (accounting for chip gaps).

For a full overview of all the neutrino alerts followed up as part of our program, see Table VI. ANTARES did not report any neutrinos from the same direction [5], though the corresponding upper limits reported are not constraining for the neutrino production models introduced in this work.

AT2019fdr, at a location of RA[J2000] = 257.2786 and Dec[J2000] = +26.8557, was lying within the 90% localization region of IC200530A. It was consistent with arising from the nucleus of its host galaxy (SDSSCGB 6856.2), with a mean angular separation to the host position as reported in *Gaia* Data Release 2 [6] of 0.03 ± 0.15 arcsec. The angular separation from the neutrino best fit position was 1.72 deg. The event had a spectroscopic redshift of $z = 0.267$, which implies a luminosity distance $D_\mathrm{L} \approx 1360$ Mpc, assuming a flat cosmology with $\Omega_\Lambda = 0.7$ and $H_0 = 70$ km s^{-1} Mpc^{-1}.

Gamma ray limits   Details on the *Fermi*-LAT analysis and the upper limits can be found in [7]. The High Altitude Water Cherenkov Experiment (HAWC) reported that no significant detection was found at the time of neutrino arrival [8]. A non-detection was also reported by the International Gamma-Ray Astrophysics Laboratory (INTEGRAL) [9].

X-ray observations   In the course of its ongoing all sky survey, the *SRG* observatory [10] visited AT2019fdr four times with its 6 month cadence, the first visit having taken place on 2020, March 13–14. The source was detected by eROSITA [11] only once, during the third visit on 2021, March 10–11, providing evidence for temporal evolution in the X-ray emission of the source. Constraints on the flux from all three epochs are shown in Fig. 1 and listed in Table I.

The single detection of AT2019fdr revealed a very soft thermal spectrum with a best-fit blackbody tempera-

MJD	Date	Upper limit (95% CL) [erg s^{-1} cm^{-2}]	Energy flux [erg s^{-1} cm^{-2}]
58922	2020-03-14	2.5×10^{-14}	–
59105	2020-09-13	2.9×10^{-14}	–
59284	2021-03-11	–	$6.2^{+2.7}_{-2.1} \times 10^{-14}$
59465	2021-09-08	5.3×10^{-14}	–

TABLE I. *SRG*/eROSITA detection and upper limits in the 0.3–2.0 keV band.

ture of 56^{+32}_{-26} eV (errors are 68% for one parameter of interest). In the rest frame of the source this corresponds to a temperature of 71^{+41}_{-33} eV and is among the softest X-ray spectra of all TDEs so far detected by *SRG*/eROSITA [12]. The best fit value of the equivalent hydrogen column density NH = $1.47^{+2.80}_{-1.25} \times 10^{21}$ cm^{-2} is consistent, within the errors, with the Galactic value of NH$_\mathrm{Gal}$ = 0.40×10^{21} cm^{-2} [13]. As is usually the case for soft sources, there is some degree of degeneracy between the neutral hydrogen column density and the temperature. However, the upper bound on the temperature is still fairly low, $T_\mathrm{bb} < 131$ eV at the 95% confidence level.

Prior to the detection of IC200530A, *Swift*-XRT had already observed AT2019fdr on 14 occasions [14]. Following the identification of AT2019fdr as a candidate neutrino source, an additional prompt ToO observation of the object was requested, which was conducted on 2020, June 7 (2000 second exposure).

To reduce the data and generate a lightcurve, the publicly available `Swift XRT data products generator` [15] was used for the energy range 0.3–10 keV. Further details can be found at [16]. Since the event was not detected in any individual XRT pointings, the 14 observations prior to neutrino arrival were binned (20700 seconds in total) to compute a 3σ energy flux upper limit of 1.4×10^{-13} erg s^{-1} cm^{-2}. The observation after neutrino arrival yielded a 3σ energy flux upper limit of 4.7×10^{-12} erg s^{-1} cm^{-2}. To convert photon counts to energy flux, the `HEASARC WebPIMMS` tool [17] was employed, using the *SRG*/eROSITA blackbody temperature of 56 eV. Absorption was corrected with the best-fit equivalent hydrogen column density from the same measurement (see above).

Optical/UV observations   The ZTF observations were analyzed using dedicated forced photometry, yielding higher precision than 'alert' photometry by incorporating knowledge of the transient's position derived from all available images. This was done using the `ztffps` pipeline [18], which is built upon `ztflc` [19].

To obtain *Swift* measurements, we retrieved the science-ready data from the *Swift* archive (https://www.swift.ac.uk/swift_portal). We co-added all sky exposures for a given epoch and filter to boost the signal-to-noise ratio using `uvotimsum` in HEAsoft (https://heasarc.gsfc.nasa.gov/docs/

software/heasoft/, v6.26.1). Afterwards, we measured the brightness of the transient with the *Swift* tool uvotsource. The source aperture had a radius of 3 arcsec, while the background region had a significantly larger radius. The photometry was calibrated with the latest calibration files from September 2020 and converted to the AB system using the methods of Breeveld *et al.* [20]. All measurements were host subtracted using the synthetic host model described in the next section.

Infrared observations Four epochs of observations were taken in the J-, H- and Ks-band with the WIRC camera [21] mounted on the Palomar P200 telescope in 2020 on July 1 and September 27, as well as in 2021 on February 2 and May 28. The WIRC measurements were reduced using a custom pipeline described in [22]. This pipeline performs flat fielding, background subtraction and astrometry (with respect to Gaia DR2) on the dithered images followed by stacking of the individual frames for each filter and epoch. Photometric calibration was performed on the stacked images using stars from the Two Micron All Sky Survey (2MASS) [23] in the WIRC field to derive a zero point for the stacked images.

The combined host and flare flux was extracted from the stacked images using GALFIT [24] to avoid contamination from blending with a close neighboring galaxy. photutils [25] was used to derive the Point Spread Function (PSF) for each image. For this purpose, 3–5 isolated stars which were neither dim nor bright were selected by visual inspection of the surrounding area. Based on these, the PSF in the images was fitted. The subtraction quality was verified through visual inspection of the residuals of 4 nearby reference stars from the Sloan Digital Sky Survey (SDSS) [26]. Following this, Sérsic profiles were fitted to AT2019fdr's host galaxy and to the neighboring galaxy. Additionally, a point source was fitted.

All parameters except the point source flux were fixed after fitting one epoch (reference epoch). The point source flux was then fit in the other epochs. As the choice of reference epoch had an impact on the flux estimate, both the first and the last epoch were used as such. The difference in the point source flux estimate between both was taken to serve as the systematic uncertainty.

The host galaxy flux was estimated by fitting a galaxy model following the method of van Velzen *et al.* [27]. The UV flux was measured with images from the Galaxy Evolution Explorer (*GALEX*) [28], using the gPhoton software [29] with an aperture of 4 arcsec. The optical flux of the host was obtained from the SDSS model magnitudes [30]. The baseline *WISE* data points mentioned above were also included, as was an archival measurement from the UKIRT Infrared Deep Sky Survey (UKIDSS) [31]. The prospector software was employed to sample synthetic galaxy models built by Flexible Stellar Population Synthesis (FSPS, [32, 33]). An overview of the values used for constructing the model can be seen in Table III.

In addition to the ground-based NIR observations,

photometry was extracted from MIR images of the *WISE* [34] satellite. For this the W1- and the W2-band were used, centered at 3.4 and 4.6 μm, respectively. The *WISE* and *NEOWISE* (the new designation after a hibernation period, [35]) photometry at the location of AT2019fdr suffered from blending with a nearby galaxy, so forced PSF photometry was used [36] on the co-added images [37]. These images were binned in 6 month intervals, aligned to the observing pattern of the satellite. The *WISE* flux in the 13 epochs prior to the optical flare was used to define a baseline, from which difference flux was then computed. We measured a significant flux increase from this baseline. In the W1-band, the root mean square (RMS) variability of the baseline was only 18 μJy , which is much smaller than the peak difference flux of 0.9 mJy.

The infrared brightness over time, as detected by P200 and *WISE* after subtracting the host baseline contribution, is shown in Table II.

A selection of IR, optical and UV data are shown in Figure 1, alongside upper limits from *Swift*-XRT and *Fermi*-LAT, as well as the measurements from *SRG*/eROSITA.

Radio observations We observed AT2019fdr with a dedicated Karl G. Jansky Very Large Array (VLA) Director's Discretionary Time (DDT) program VLA/20A-566 (PI: Stein), and obtained multi-frequency detections at three epochs. The individual observations were taken in 2020 on July 3, September 13 and November 7. The array was in its moderately-extended B configuration for the first two observations, and in the hybrid BnA configuration (with a more extended northern arm) for the final epoch. The first observation was performed in the 2–4 and 8–12 GHz bands, to which we added the 1–2 and 4–8 GHz bands in the subsequent epochs. We used 3C 286 for the delay, bandpass, and flux calibration, and the nearby source J1716+2152 for the complex gain calibration. We followed standard procedures for the external gain calibration, which were performed with the VLA calibration pipeline, using the Common Astronomy Software Application (CASA) v5.6.2. The source was then imaged in each observed band with the CASA task tclean, using Briggs weighting with a robust factor of 1 as a compromise between sensitivity and resolution. The target flux density was measured by fitting a point source in the image plane.

While consistent flux densities were measured in the 2–4 and 8–12 GHz bands in the first two observations, the final epoch suggested a possible spectral steepening, with reduced flux densities in the 4–8 and 8–12 GHz bands (see Fig. 2). However, extensive testing revealed that this apparent spectral steepening was not intrinsic to the source. We interpolated the gains derived on the first, third and last of the five 8–12 GHz scans on J1716+2152 to the remaining two scans, deriving their calibration in the same way as for AT2019dsg (see [38]). The measured calibrator flux densities for those two scans were found to

MJD	Date	J-band	H-band	Ks-band
59031	2020-07-01	19.06 ± 0.50	17.73 ± 0.12	17.13 ± 0.26
59121	2020-09-29	19.78 ± 0.98	17.76 ± 0.12	17.45 ± 0.35
59249	2021-02-04	–	18.26 ± 0.19	17.81 ± 0.48
59362	2021-05-28	–	18.42 ± 0.22	17.91 ± 0.53
		W1-band	**W2-band**	
58709	2019-08-14	17.18 ± 0.11	17.08 ± 0.23	
58910	2020-03-02	16.49 ± 0.07	16.37 ± 0.11	
59074	2020-08-13	16.47 ± 0.09	16.20 ± 0.11	

TABLE II. *Top*: NIR AB magnitudes after subtraction of the synthetic host model. Only systematic uncertainties are given (photometric uncertainties should be negligible in comparison, at least in the J- and H-band). The third and fourth J-band epochs had negative flux after host-model subtraction, which are counted as non-detections. *Bottom*: MIR AB magnitudes after subtracting the pre-peak baseline.
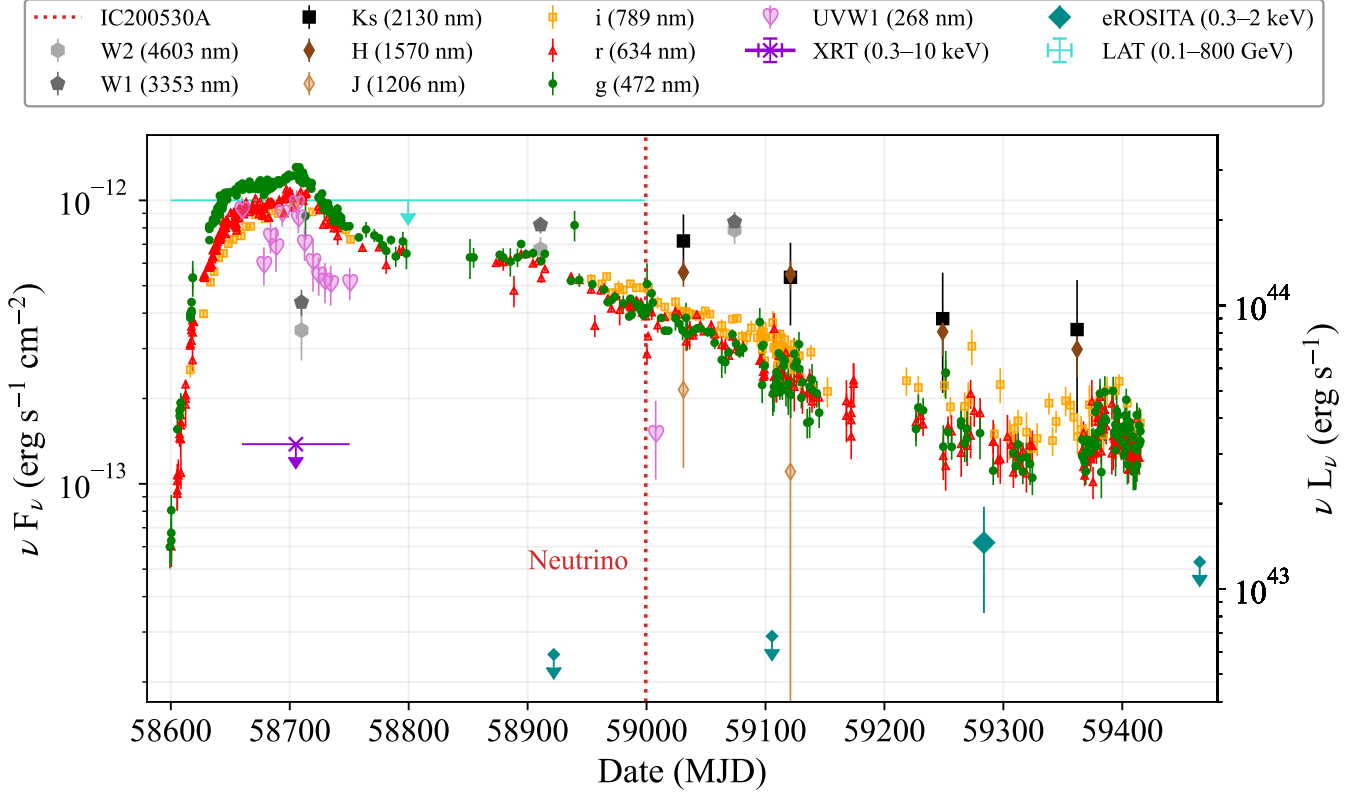

FIG. 1. Lightcurve of AT2019fdr, showing host-subtracted ZTF, *WISE*, P200 and *Swift*-UVOT photometry, non host-subtracted *SRG*/eROSITA photometry, as well as binned *Swift*-XRT and *Fermi*-LAT upper limits (the former has been corrected for absorption). The X-ray and gamma ray data is given in units of integrated flux. The dotted vertical line indicates the arrival time of the IceCube neutrino IC200530A.

be significantly lower than for the other three. This implied significant atmospheric phase changes between calibrator scans, which reduced the measured flux densities due to decorrelation. Without sufficient flux density in the target field to apply self-calibration, we were unable to correct for this effect, which is worst at the highest frequencies. Therefore, no evidence for intrinsic source variability can be found in the radio band across the 5 months of observations.

Additionally, an archival upper limit was obtained from the Very Large Array Sky Survey (VLASS) [39], which was the only sky survey with adequate sensitivity and angular resolution to probe the emission on the angular and flux density scales relevant for AT2019fdr. The quicklook continuum fits image for tile T17t23We was downloaded from the archive (https://archive-new.nrao.edu/vlass/quicklook/) and dates to 2017, November 25 (2–4 GHz band). No emission was

Band	AB magnitude
GALEX FUV	$22.32^{+0.07}_{-0.10}$
GALEX NUV	$21.52^{+0.06}_{-0.10}$
SDSS u	$20.91^{+0.06}_{-0.07}$
SDSS g	$19.97^{+0.04}_{-0.04}$
SDSS r	$19.00^{+0.02}_{-0.03}$
SDSS i	$18.64^{+0.02}_{-0.03}$
SDSS z	$18.36^{+0.02}_{-0.03}$
UKIRT J	18.18
WISE W1	$17.83^{+0.05}_{-0.05}$
WISE W2	$17.78^{+0.03}_{-0.05}$

TABLE III. Archival measurements from *GALEX*, SDSS, UKIRT (the isoMag value was given without error) and *WISE*. These were used to build the synthetic host model.

detected at a 3σ significance, where $\sigma = 0.11$ mJy/beam is the local RMS noise and the beam is 2.46 arcsec $\times$ 2.28 arcsec (position angle $= -37°$), resulting in an upper limit of 0.32 mJy. This result is fully consistent with what was measured in the same band in our dedicated observations. A more recent observation from VLASS epoch 2 was taken very close to the second dedicated observation (2020, September 6), but the local noise was slightly larger and the 3σ upper limit was less constraining (0.4 mJy).

All our measurements, as well as the archival limit from VLASS are shown in Fig. 2 and Table IV.

The observed radio spectra can be described by synchrotron emission from a population of relativistic electrons. These electrons were assumed to be accelerated into a power-law distribution in energy, which leads to a power law in the unattenuated synchrotron spectrum. No break in the power-law spectrum was observed. Therefore the peak frequency, where synchrotron self-absorption sets in, is expected to lie below the lowest observed frequency. The data was analyzed using the models from [38, 40]. This allowed to infer energies of a few times 10^{50} erg for the electron population, under the assumption of equipartition; a peak flux of 0.5 mJy at 1 GHz; and neglecting the impact of baryons. This value provides a lower limit on the non-thermal energy of the system. Given that electrons are typically accelerated with much lower efficiency than protons in astrophysical accelerators [41], they were assumed to carry 10% of the energy carried by relativistic protons ($\epsilon_e = 0.1$). Furthermore, the magnetic field was assumed to carry 0.1% of the total energy ($\epsilon_B = 10^{-3}$), as indicated by radio observations of TDEs [42] and supernovae [43]. Under these assumptions, the total energy energy in non-thermal particles was inferred to be $\sim 10^{52}$ erg. The inferred size of the emission region, $\sim 10^{18}$ cm, and the lack of temporal evolution suggest that the emission was primarily powered by an outflow that was active already prior to
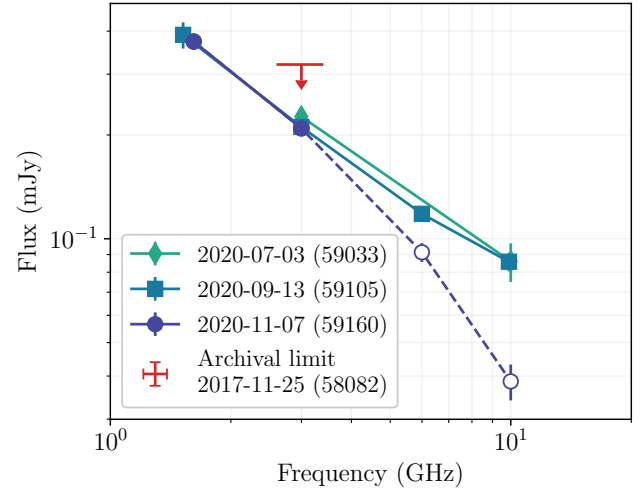

FIG. 2. Three epochs of VLA measurements of AT2019fdr, as well as the VLASS archival upper limit. Note: The apparent spectral steepening in our third epoch (empty circular markers) appears not to be intrinsic to the source, but due to systematic effects.

MJD	Date	Band [GHz]	Flux density [μ Jansky]
58032	2017-11-25	3.00	≤ 320
59033	2020-07-03	3.00	226 ± 13
59033	2020-07-03	10.00	86 ± 11
59105	2020-09-13	1.52	390 ± 34
59105	2020-09-13	3.00	211 ± 10
59105	2020-09-13	6.00	118 ± 6
59105	2020-09-13	10.00	86 ± 5
59160	2020-11-07	1.62	373 ± 20
59160	2020-11-07	3.00	209 ± 9
59160	2020-11-07	6.00	91 ± 6
59160	2020-11-07	10.00	39 ± 5

TABLE IV. VLA measurements and the VLASS archival limit (first row).

the transient event. A second, sub-dominated component could be present. Since the radio observations cover only a period of 5 months, a fast-varying transient signal would be easier to constrain than a slower one. For instance, a relativistic jet viewed face-on would show faster variations and dominate the radio flux if sufficiently energetic, while an off-axis relativistic jet could escape detection due to Doppler deboosting of its radio flux (the latter explanation only works up to the point the jet decelerates and starts to emit isotropically, see e.g. [44]).

Double-blackbody fit The SED was fit using the `lmfit` Python package [45] with both a broken and a non-broken intrinsic power law, as well as a single and a double unmodified blackbody spectrum. The data are well described by a double-blackbody model, comprised of an optical/UV 'blue' blackbody and an infrared 'red' blackbody. Fitting is done for three epochs during which

Epoch	Band	Temp.	Radius	Luminosity
		[K]	[cm]	[erg s^{-1}]
1	O+UV	13526^{+569}_{-574}	$7.8^{+0.4}_{-0.4} \times 10^{15}$	$1.4^{+0.1}_{-0.1} \times 10^{45}$
	IR	1505^{+421}_{-313}	$2.2^{+1.6}_{-1.4} \times 10^{17}$	$1.7^{+2.2}_{-1.0} \times 10^{44}$
2	O+UV	11731^{+663}_{-683}	$4.9^{+0.4}_{-0.4} \times 10^{15}$	$3.3^{+0.3}_{-0.3} \times 10^{44}$
	IR	1762^{+121}_{-124}	$2.5^{+0.2}_{-0.2} \times 10^{17}$	$4.3^{+0.5}_{-0.7} \times 10^{44}$
3	O+UV	10230^{+2373}_{-1645}	$4.3^{+3.3}_{-1.0} \times 10^{15}$	$1.5^{+1.2}_{-0.4} \times 10^{44}$
	IR	2237^{+402}_{-462}	$1.0^{+0.6}_{-0.4} \times 10^{17}$	$1.9^{+1.4}_{-0.5} \times 10^{44}$

TABLE V. Blackbody fit values for three epochs (1–3), where 'O+UV' denotes the blue blackbody in the optical/UV and 'IR' denotes the red infrared blackbody. The luminosity is given dereddened and in the source frame and the uncertainties are at 68% confidence level. Note that the O+UV temperature and radius (and therefore the luminosity) in the third epoch are not well constrained, as there are no late-time UV measurements available. The same holds true for the infrared blackbody in the first and the last epoch, as only 2 data points are available in the infrared.

infrared, optical and UV data is available. These epochs in MJD are: 1) 58700–58720, 2) 59006–59130 and 3) 59220–59271. To account for host extinction, we employed `extinction` [46] using the Calzetti attenuation law [47]. The extinction parameter A_V was left free in epoch 1 and was fixed at the epoch 1 best-fit value ($A_V = 0.45^{+0.14}_{-0.14}$ mag for $R_V = 3.1$) for epochs 2 and 3. We chose epoch 1 to determine the extinction parameter because the observations of the optical/UV are most precise there.

The other fit parameters were the blackbody temperature and the the blackbody radius, resulting in a total of 6 fit parameters in epoch 1, and 4 in epochs 2 and 3. The model was fitted to the data in the three epochs using the Levenberg-Marquardt minimization algorithm. 68% confidence levels for all parameters were estimated by determining $\Delta\chi^2 = 1$ relative to the best-fit χ^2, stepping through each parameter while leaving the other parameters free during minimization.

The best fit blackbody values are shown in Table V; the respective SEDs for the three epochs are shown in the top panels of Fig. 1 in the main text. Note that the apparent dust temperature increase from epoch 2 to 3 is neither significant nor expected. Rather, there are no constraints by *WISE* measurements in the last epoch, pushing the dust temperature up (when removing the *WISE* datapoints from epoch 2 and redoing the fits, the temperature of the red blackbody increases to a value comparable to epoch 3).

Dust echo model and energy output Following the procedure in [48], the optical lightcurve was convolved with a rectangular function of width $2 \times \Delta t_c$, where Δt_c is the light travel time from the transient to the surrounding dust region. A best-fit value of $\Delta t_c = 193$ days was obtained, which translates to a distance to the dust region of 5×10^{17} cm (0.16 pc). To obtain a measure for the peak luminosity of the transient, the blue blackbody fit at peak was used. The resulting unobscured peak luminosity from the blue blackbody was $L_{\mathrm{peak}} = 1.4^{+0.1}_{-0.1} \times 10^{45}$ erg s^{-1}. To check this value for consistency, the peak optical/UV luminosity was also calculated following [48]. This method relies only on the blackbody temperature (normalized to 1850 K) and the radius of the dust region, normalized to 0.1 pc (assuming a dust grain size of 0.1 μm):

$$L_{\mathrm{peak}} = 5 \times 10^{44} R_{0.1}^2 T_{1850}^{5.8} \ \mathrm{erg\,s^{-1}}$$

This yielded a value of $L_{\mathrm{peak}} = 1.3 \times 10^{45}$ erg s^{-1}, which is in good agreement with the value derived from the blackbody fit described in the section above.

As the temperature of the optical/UV blackbody decreases only slightly and stays roughly centered on the g-band, the total energy radiated in the optical/UV can be approximated by scaling the peak luminosity with the g-band lightcurve and integrating over time. The resulting energy output was $E_{\mathrm{O+UV}} = 3.4 \times 10^{52}$ erg.

The peak dust echo luminosity was inferred from the IR blackbody fit to be $L_{\mathrm{dust}} = 4.3 \times 10^{44}$ erg s^{-1}. Similarly to the optical/UV, we time-integrated the fitted dust echo lightcurve, normalized to the peak dust echo luminosity from epoch 2, to obtain the total bolometric energy of the dust echo: $E_{\mathrm{dust}} = 1.1 \times 10^{52}$ erg. The ratio of the two time-integrated energies resulted in an unusually high covering factor of 1/3, while the TDE dust echoes in quiescent galaxies typically show covering factors of around 1% [48]. From the covering factor and the radius of the dust shell the dust mass can be estimated. Assuming a grain size of 0.1 μm, spherical dust grains and a typical mass density of 2.5 g cm^{-1} results in a dust mass of 0.017 $M_\odot$. This corresponds to 1.7 $M_\odot$ in gas, assuming a typical mass-to-gas ratio of 1:100.

Black hole mass The commonly adopted method to derive the mass of the central SMBH (M_{BH}) of an AGN is using its optical spectrum and is called the single-epoch virial technique (see e.g. [49]). The NOT spectrum used for this was taken on 2020, April 30 with the ALFOSC camera. There are later spectra, but these do not contain the Hα emission line. The spectrum was reduced in a standard way, consisting of wavelength calibration through an arc lamp and flux calibration using a spectrophotometric standard star.

The publicly available multi-component spectral fitting tool `PyQSOFit` [50] was used for spectral analysis. We brought the spectrum to the lab frame and dereddened it using the Milky Way extinction law of [51] with $R_V = 3.1$ and dust map data adopted from [52] – note that the extinction law is not the same as the one used in the blackbody fits, but the difference is small. The continuum was modeled using line-free regions as a combination of a third degree polynomial and an optical Fe II template adopted from [53]. It was subtracted from

the spectrum to obtain the line spectrum only. The Hα and Hβ line complexes were then fitted separately, while simultaneously fitting the emission lines in each complex. In the wavelength range of [6400,6800] Å, the Hα emission line was modeled with three Gaussian functions, two for the broad components and one for the narrow. [N II] $\lambda\lambda$6548,6584, and [S II] $\lambda\lambda$6717,6731 were also fitted with a single Gaussian. The Hβ emission line was fitted in the wavelength range [4700,5100] Å, similar to the Hα line. Finally, the [O III] $\lambda\lambda$4959,5007 doublet was modeled with two Gaussian functions. The estimated uncertainties are statistical only and do not include the intrinsic scatter ($0.3-0.4$ dex) associated with the virial approach (see e.g. [49, 54]). Further details about the fitting technique and `PyQSOFit` can be found in [55] and [56]. The fitted spectrum is shown in Figure 3.

The measured full-width-at-half-maximum (FWHM) of the Hβ line was 1914 ± 282 km s^{-1} and the continuum luminosity at 5100 Å was $\lambda L_\lambda = 44.16 \pm 0.01$ (log-scale, erg s^{-1}). Broadening due to limited detector resolution was considered to be small. From the estimated FWHM and λL_λ, the mass of the central black hole was computed by adopting the following empirical relation [54]:

$$\log\left(\tfrac{M_{\mathrm{BH,vir}}}{M_\odot}\right) = a + b\log\left(\tfrac{\lambda L_\lambda}{10^{44}\,\mathrm{erg/s}}\right) + 2\log\left(\tfrac{\mathrm{FWHM}}{\mathrm{km/s}}\right)$$

The coefficients a and b were taken as 0.91 and 0.5, adopted from [49]. This resulted in $M_{\mathrm{BH}} = 10^{7.55 \pm 0.13} M_\odot$. [54] also give the following empirical relation to estimate M_{BH} from the Hα line FWHM and luminosity:

$$\log\left(\tfrac{M_{\mathrm{BH,vir}}}{M_\odot}\right)_{\mathrm{H}\alpha} = 0.379 + 0.43\log\left(\tfrac{L_{\mathrm{H}\alpha}}{10^{42}\mathrm{erg/s}}\right) + 2.1\log\left(\tfrac{\mathrm{FWHM}_{\mathrm{H}\alpha}}{\mathrm{km/s}}\right)$$

Supplying the derived H$_\alpha$ FWHM (1753 ± 246 km s^{-1}) and luminosity (43.05 ± 0.06, log-scale, erg s^{-1}) in the above equation, M_{BH} was computed as $10^{7.64 \pm 0.13} M_\odot$, consistent with the previous estimate.

These estimates are consistent with the masses derived in the NLSy1 ZTF study [14], which employed two different methods. The virial approach (also used above) yielded an estimate of $10^{7.1} M_\odot$, while an approach using the host galaxy luminosity according to [57] resulted in $10^{7.8} M_\odot$. In this paper an Eddington ratio of $\frac{L}{L_{\mathrm{Edd}}} = 0.24 - 1.2$ was derived. The different result for the virial approach can be explained by the fact that [14] fit a single Lorentzian profile while here a multi-Gaussian approach is used. Also, the spectrum employed for the fit presented here was more recent, presumably containing less transient emission.

Chance coincidence To compute the chance coincidence of finding an event like AT2019fdr in association with a high-energy neutrino, we obtained the full set of nuclear ZTF transient flares as selected by AMPEL [2, 58] from the ZTF alert stream [59]. At least 10 detections in both g- and r-band were required, as was a weighted host–flare offset ≤ 0.5 arcsec and a majority of the data points having positive flux after subtracting the reference image. The dataset was further restricted to transients being first detected after 2018 January 1 and peaking before July 2020. 3172 flares survived these cuts.

We further required the nuclear transients not to be classified as (variable) star or bogus object (e.g. subtraction artifacts); additionally, flares were rejected when their rise (fade) e-folding time (see [60] for details) was smaller than the uncertainty on this value; these two cuts left 1628 candidates. As we were only interested in events of brightness comparable to AT2019fdr, we required that the peak apparent magnitude (see [7] for details) $\leq$ the peak magnitude of AT2019fdr; this left 157 events. Furthermore, the rise (fade) e-folding time was required to be in the [15, 80] ([30, 500]) day interval to select for (candidate) TDEs, resulting in 25 transients.

Nuclear transients which have been spectroscopically classified as supernovae were excluded from the remaining 25 events. Furthermore, we visually excluded transients showing only short-timescale AGN variability, displaying no consistent color or color evolution and events which were not sufficiently smooth post peak. This procedure left a final sample of 12 transients.

To calculate the effective source density of these 12 events, their lifetime was conservatively estimated at 1 year per event. The ZTF survey footprint is $28000\,\mathrm{deg}^2$ (excluding sources with galactic latitude $|b| < 7$) [38]. From the time range of the sample (2.5 years) and the ZTF footprint, the effective source density was computed as $1.7 \times 10^{-4}\,\mathrm{deg}^{-2}$. This is the density of sources per deg^2 of sky in the survey footprint at any given time. Through multiplying the effective source density by the combined IceCube alert footprint of $154.3\,\mathrm{deg}^2$, an expectation value for the number of neutrinos can be calculated. Employing a Poisson distribution, the chance coincidence of finding 2 sources by chance was calculated as $p = 3.4 \times 10^{-4}$ ($p = 2.6 \times 10^{-2}$ for one source only).

Disk-corona model Accretion disks and their coronae have been proposed as neutrino production sites (see [115]). The plasma is expected to be collisional for standard disks and slim disks. In particular, for super-Eddington disks, the proton-electron relaxation time is shorter than the infall time, leading to $kT_e \approx kT_p$. So sub-PeV neutrino production inside accretion disks including those from super-Eddington magnetically arrested disks [116] are highly suspicious for this TDE. On the other hand, it has been shown that the plasma can be collisionless for highly magnetized regions such as disk-coronae and radiatively inefficient accretion flows [117, 118]. Not only magnetic reconnections but also the Fermi acceleration mechanism may operate if the plasma density is not too large to be collisionless. This work focuses on neutrino emission from the coronae.
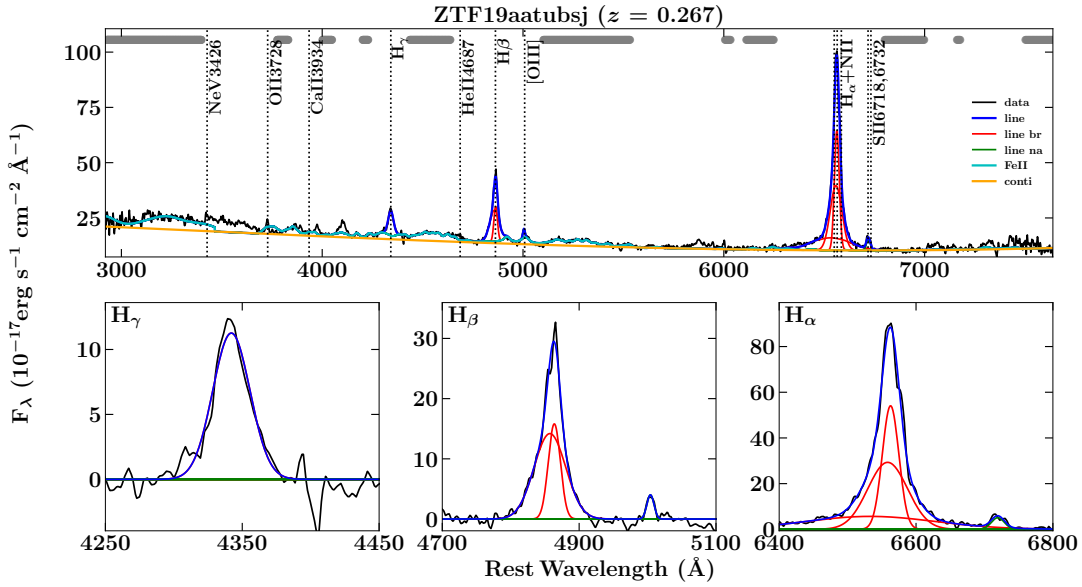
FIG. 3. The top plot shows the NOT spectrum of AT2019fdr analyzed with `PyQSOFit`; different line components are labeled. The bottom panels show zoomed versions of the fitted line complexes.

Following [115], we calculated the neutrino emission from coronae above the TDE disk. The size of the coronal region was assumed to be $R = 30\,R_S$, where R_S is the Schwarzschild radius, the alpha viscosity was set to $\alpha = 0.1$, and the plasma β was assumed to be $\beta = 0.2$. Spectral energy distributions were determined by the optical and ultraviolet luminosity, $\nu F_\nu = 10^{-12}\ \mathrm{erg\ cm^{-2}\ s^{-1}}$. This is consistent with a bolometric luminosity of $L \sim 10^{45}$ erg s^{-1}, which leads to the Eddington ratio $\lambda_{\mathrm{Edd}} \equiv L_{\mathrm{bol}}/L_{\mathrm{Edd}} \sim 0.3$ (the accretion is near the Eddington limit, and super-Eddington accretion is often characterized by $\lambda_{\mathrm{Edd}} \gtrsim 1$ [119–121]). The corresponding Comptonized X-ray luminosity was around a few 10^{43} erg s^{-1}, which can be reprocessed by the TDE debris.

Neutrinos and gamma rays can be efficiently produced by both $p\gamma$ and pp interactions [117]. Here the `SOPHIA` Monte Carlo code [122] was used to simulate neutrino spectra from $p\gamma$ interactions. For non-thermal protons, stochastic acceleration was assumed, although magnetic reconnections may also be considered. The acceleration time is given by $t_{\mathrm{acc}} \approx \eta_B (c/V_A)^2 (H/c)(r_L/H)^{2-q}$, where V_A is the Alfvén velocity, H is the scale height, and r_L is the Larmor radius. We used $\eta_B = 10$ and $q = 5/3$.

The cosmic ray luminosity was normalized by the cosmic ray pressure, for which $P_{\mathrm{CR}} = 0.5 n_p k_B T_p$ was used, where n_p is the proton density and the proton temperature T_p was assumed to be the virial temperature. This gives a reasonable upper limit in accretion flow models. The expected number of muon neutrinos under the effective area of the neutrino alert channel is ~ 0.007. The peak neutrino energy depends on β, and the observed

energy of ~ 80 TeV can be achieved even for $\beta \sim 0.5 - 1$. Note that in general the cosmic ray luminosity is expected to be less than the optical/UV accretion disk luminosity, $L_{\mathrm{CR}} \lesssim L$ because of $\eta_{\mathrm{CR}} \lesssim \eta_{\mathrm{rad}}$.

In this model, there are two explanations for the time delay between optical peak and neutrino detection [115]. The accretion at the earliest phase may be super-Eddington, but it will enter the sub-Eddington regime as the accretion rate decreases. Recent magnetohydrodynamic simulations have shown that high-temperature coronal regions form above the accretion disk [123, 124]. The neutrino observation time can be consistent with the formation time of the collisionless corona. Alternatively, the corona may form even in the super-Eddington phase [125], with the neutrino luminosity being initially saturated and tracing the accretion history at late times.

Sub-relativistic wind model Non-relativistic outflows provide natural sites for high-energy neutrino and gamma-ray production. It has been believed that a TDE event is accompanied by the formation of an accretion disk, launching disk-driven winds with a velocity of $V_w \sim 0.1c$. The observed optical emission could be reprocessed emission of shocked dissipation by the wind [126–128] and the launch of radiation-driven winds has been supported by numerical simulations (e.g. [120]).

Self-interactions between tidal streams and/or collisions between the wind and TDE debris would lead to a strong shock, in which particles (both ions and electrons) can be accelerated. If the magnetic field energy density is $U_B \equiv \epsilon_B L_w/(4\pi R_w^2 V_w)$, then $\epsilon_B \sim 0.03$, a wind kinetic luminosity of $L_w \sim 10^{45.5}$ erg s^{-1} and

Event	R.A. (J2000) (deg)	Dec (J2000) (deg)	90% area (deg^2)	ZTF obs (deg^2)	Signal-ness	Reference
IC190503A	120.28	6.35	1.94	1.37	36%	[61, 62]
IC190619A	343.26	10.73	27.21	21.57	55%	[63, 64]
IC190730A	225.79	10.47	5.41	4.52	67%	[65, 66]
IC190922B	5.76	−1.57	4.48	4.09	51%	[67–69]
IC191001A	314.08	12.94	25.53	23.06	59%	[70–72]
IC200107A	148.18	35.46	7.62	6.28	−	[73, 74]
IC200109A	164.49	11.87	22.52	22.36	77%	[75, 76]
IC200117A	116.24	29.14	2.86	2.66	38%	[77–79]
IC200512A	295.18	15.79	9.77	9.26	32%	[80, 81]
IC200530A	**255.37**	**26.61**	**25.38**	**22.05**	**59%**	[82–85]
IC200620A	162.11	11.95	1.73	1.24	32%	[86, 87]
IC200916A	109.78	14.36	4.22	3.61	32%	[88–90]
IC200926A	96.46	−4.33	1.75	1.29	44%	[91, 92]
IC200929A	29.53	3.47	1.12	0.87	47%	[93, 94]
IC201007A	265.17	5.34	0.57	0.55	88%	[95, 96]
IC201021A	260.82	14.55	6.89	6.30	30%	[97, 98]
IC201130A	30.54	−12.1	5.44	4.51	15%	[99, 100]
IC201209A	6.86	−9.25	4.71	3.20	19%	[101, 102]
IC201222A	206.37	13.44	1.54	1.40	53%	[103, 104]
IC210210A	206.06	4.78	2.76	2.05	65%	[105, 106]
IC210510A	268.42	3.81	4.04	3.67	28%	[107, 108]
IC210629A	340.75	12.94	5.99	4.59	35%	[109, 110]
IC210811A	270.79	25.28	3.17	2.66	66%	[111, 112]
IC210922A	60.73	25.28	-4.18	1.16	93%	[113, 114]

TABLE VI. Summary of the 24 neutrino alerts followed up by ZTF until September 2021, with IC200530A highlighted. The 90% area column indicates the rectangular uncertainty region of sky as reported by IceCube. The ZTF obs column indicates the area observed at least twice by ZTF, within the reported 90% localization (accounting for chip gaps). *Signalness* estimates the probability that the neutrino is of astrophysical origin, rather than caused by atmospheric background. The total followed-up area (corrected for chip-gaps) is 154.33 deg^2.

a termination shock radius of $R_w \sim 10^{16}$ cm lead to $B_w \sim 30$ G and a maximum proton energy of 25 PeV in the presence of $p\gamma$ energy losses. Then, cosmic rays leaving the wind interact with the TDE debris via inelastic pp collisions. For a TDE event of a main-sequence star with $\sim 1\ M_\odot$, the effective optical depth for neutrino production is nearly unity at the assumed dissipation radius, $R_{\rm diss} = R_w = 10^{16}$ cm, in which the system is approximately calorimetric for neutrino and gamma-ray production [115]. We use the optical/UV luminosity $L = 1.4 \times 10^{45}$ erg s^{-1} from the blackbody fit and $L_X = 0.03\,L$, although in this model the results are not sensitive to X-rays. The magnetic field is set to $B_w = 30$ G.

The cosmic ray luminosity was normalized by the baryon loading factor, $\xi_{\rm CR} = L_{\rm CR}/L$. For $\xi_{\rm CR} = 3$, the expected number of neutrino events was ~ 0.002 under the effective area of the neutrino alert channel. The resulting neutrino spectrum consists of pp and $p\gamma$ components, and there is a dip around ~ 100 TeV caused by the Bethe-Heitler pair production due to optical and ultraviolet photons. In this model, the neutrino light curve is expected to trace the kinetic luminosity as long as the system is calorimetric [115].

Jet model Following Winter and Lunardini [129], we considered a relativistic jet, where the beamed neutrino emission allows to naturally meet the energy requirement. In the absence of X-ray signatures before and near the neutrino detection time, the model has been based on a TDE unified model [130].

The interpretation of TDE X-ray signals over a wide range of SMBH masses has been the subject of a recent series of papers [131–134]. In short, for higher SMBH masses, lower X-ray temperatures (possibly including a non-thermal tail) are expected to shift the peak of the thermal spectrum coming from the disk out of the *Swift* or *SRG*/eROSITA energy ranges. Following Mummery [133] for the temperature and luminosity dependence on these quantities, we extrapolated from the values for AT2019dsg (where $M \simeq 10^6\ M_\odot$ is assumed) to the corresponding values for $M \sim 10^7\ M_\odot$, obtaining an X-ray temperature $T_X \simeq 34$ eV and an X-ray peak luminosity $L_X \simeq 1.7 \times 10^{43}$ erg s^{-1} in the *Swift* or *SRG*/eROSITA energy windows ($L_{\rm FUV} \simeq 7 \times 10^{44}$ erg s^{-1} at the BB peak, bolometrically corrected over the full energy range). The disk X-ray luminosity was assumed to scale with the BB luminosity as well, following its lightcurve. The X-ray peak luminosity assumption is accidentally consistent with the late-time X-ray detection luminosity within uncertainties ($L_X \simeq 1.4 \times 10^{43}$ erg s^{-1} in the *SRG*/eROSITA range at MJD 59284), and it is roughly consistent with the earlier limits if a mod-

erate amount of time evolution or X-ray obscuration is assumed (which is required independent of the model). For the X-ray measurements, see Fig. 1 and Table I.

Note that it is implied that the SMBH mass for AT2019fdr is an order of magnitude larger than that of AT2019dsg. The mass ($6\,M_\odot$) and radius ($R_* \simeq 4R_\odot$) of the disrupted star were assumed to be much larger as well. This is natural considering the overall larger energy budget and longer duration of the flare, as long as the available energy is proportional to a fixed fraction of the star's mass. This assumption is also consistent with the prediction that the contribution of super-solar stars to the TDE rate increases with M [135].

Assuming that the Schwarzschild time $\tau_S \simeq 630\,\mathrm{s}\,(M_{\mathrm{SMBH}}/(10^7\,M_\odot))$ translates into the time variability of the engine, we assumed a variability timescale $t_v \simeq 1000\,\mathrm{s}$. This means that internal shocks from the intermittent engine will form at a distance (collision radius) $R_C \simeq 2\,\Gamma^2\,t_v\,c \simeq 10^{16}\,\mathrm{cm}$ for our choice of $\Gamma = 14$, which is roughly comparable to the blackbody (BB) radius at peak times, see Table V. Since t_v is proportional to the SMBH mass, a larger value of R_C was expected for AT2019fdr compared to AT2019dsg – consistent with the hypothesis of a larger system. Similar to [129], it was postulated that the production and the isotropization radius roughly evolve like the BB radius to enhance the late-time neutrino production efficiency, which means that our model follows the BB fit values from Table V (linearly interpolating, and extrapolating to constant values outside the observation epochs).

The jet luminosity was assumed to be $L_{\mathrm{jet}}^{\mathrm{phys}} \simeq 6\,L_{\mathrm{edd}}$ at the peak (slightly lower than in [130] to avoid too extreme mass estimates for the disrupted star), and evolving like the BB luminosity (see fig. 4); the resulting total energy into the jet was $\simeq 0.5\,M_\odot$, which is roughly consistent with the assumed $6\,M_\odot$ of the disrupted star.

The isotropic-equivalent non-thermal proton luminosity (thin green curve in Fig. 4) $L_p^{\mathrm{iso}} \simeq (2\,\Gamma^2)\,\varepsilon\,L_{\mathrm{jet}}^{\mathrm{phys}}$, where $(2\,\Gamma^2)$ is the beaming factor and $\varepsilon \simeq 0.2$ is the transfer (dissipation) efficiency from jet kinetic energy into non-thermal radiation (here assumed to be dominated by baryons). The jet ceases once $L_{\mathrm{jet}}^{\mathrm{phys}} \lesssim L_{\mathrm{edd}}$ (see e.g., [136, 137]). Protons were assumed to be accelerated in internal shocks to an E^{-2} spectrum with the maximal energy being obtained from comparing the acceleration rate with energy losses and escape rates. The resulting number of expected muon neutrino events is 0.027.

It is an interesting feature of the model that back-scattered (isotropized) X-rays stemming from the disk serve as external target photons. In this scenario, travel times in the system can lead to a delay of the neutrino signal from building up the external radiation field. Compared to AT2019dsg, there are several possibilities which may induce this isotropization: (sublimated) dust, an outflow, or even the broad line region. For example, if the

X-ray scattering occurs near the radius of the IR emission, the delay due to the light travel (photons traveling twice the distance, to and from the IR region) is roughly $2\,\Delta t_c \simeq 386$ days (see the section on the dust echo for details). A drawback is a large dilution factor of the external radiation field due to the size of the isotropization region. Another possible idea is that the X-rays could be efficiently back-scattered in the inner part of the durst torus by the gas produced by dust sublimation, or some fine-tuned geometry may be at play. For example, the ramp-up timescale during which the dust echo sets in points towards a smaller region, comparable to R_C, which would imply only moderate dilution – but which would come at the expense of no delayed onset of the neutrino flux. On the other hand, an outflow with $v \simeq 0.01c$ would have a similar effect satisfying both requirements (small dilution and delayed onset), similarly to what was proposed for AT2019dsg [129].

Since the TDE occured within a pre-existing Seyfert galaxy, it is also possible that the X-ray scattering occured in the broad line region similar to the suggestion by Murase et al. [138]. In the absence of further constraints, it was assumed that the external target photons build up over a timescale of $2\,\Delta t_c$ after MJD 58650 (start of the broad peak) at an isotropization radius comparable to R_C, and that the back-scattering efficiency is 0.3, which is closest to the outflow scenario. Note that if the obscuration were at play at early times (where strong X-ray limits exist, see Fig. 1) and the late-term signal was indicative for the flux, then the unobscured X-ray flux could be much higher – which would allow for a larger dilution factor.

Our results are summarized in Fig. 4 here (luminosity evolution) and Fig. 2 in the main text (neutrino fluence as a function of energy). The neutrino lightcurve predicts an average delay similar to the actual delay, although the predicted variation is large. The buildup of the neutrino lightcurve is delayed with respect to the BB because of the size of the system delaying the buildup of the external target photons. On the other hand, the late-term decrease of the production/isotropization radius sightly boosts the neutrino production efficiency. It is intriguing that the shape of the isotropized X-ray curve is very similar to the dust echo curve in Fig. 2 (main text); suggesting that the dust might play a role in the X-ray isotropization.

In comparison to AT2019dsg, the main differences in the model are the larger size of the system, the larger SMBH mass and the smaller fraction of energy going into the jet, the larger mass of the disrupted star, and a higher assumed back-scattering efficiency, because the system is expected to be covered with components of the pre-existing AGN. Furthermore, a slightly higher Γ (than AT2019dsg) was assumed and a viewing angle $\theta_v = 1/\Gamma$, such that Doppler and Gamma factors are identical (for AT2019fdr). The neutrino event rates are relatively sim-
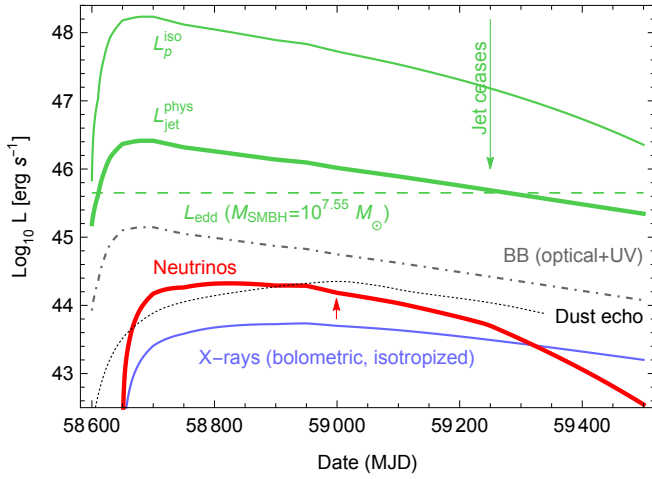
FIG. 4. Evolution of luminosities as a function of MJD. The BB curve (black-dashed) extrapolates the observed lightcurves, normalized to the O+UV luminosity at peak (see Table V). The Eddington luminosity is shown as well (green-dashed), the physical jet luminosity (thick-green) is assumed to follow the BB luminosity, peaking at $6\,L_{\rm edd}$. The isotropic-equivalent non-thermal proton luminosity $L_p^{\rm iso} \simeq (2\,\Gamma^2)\,\varepsilon\,L_{\rm jet}^{\rm phys}$, where $(2\,\Gamma^2)$ is the beaming factor and $\varepsilon \simeq 0.2$ is the transfer (dissipation) efficiency from jet kinetic energy into non-thermal radiation (here assumed to be dominated by baryons). The X-ray luminosity (purple) is the bolometric isotropized luminosity available for neutrino production. The neutrino lightcurve (red) is a result of the computation. We have marked the actual neutrino arrival time with a red arrow and show the dust echo curve from Fig. 1 (main text) for comparison.

ilar, and so are the spectra. Note that the origin of the X-ray isotropization might be different: for AT2019dsg, a mildly relativistic outflow – originally associated with the radio signal – was assumed to be the reason, since no pre-existing AGN components were expected. In the case of AT2019fdr, the scattering could also come from a similar outflow, but there is no observational evidence for that and there are the other possibilities discussed earlier. In all cases, the observed time delay of the neutrino seems to scale with the size of the system.

It has been established that relativistic jets lead to radio afterglow emission. In the case of AT2019dsg, the radio data are best explained by sub-relativistic winds in the standard leptonic emission scenario rather than a relativistic jet [139, 140]. The origin of the radio emission from AT2019fdr is uncertain, and there is no evidence for a jet. In this regard, [115] examined a hidden jet model by requiring that the relativistic jet is choked such that afterglow emission does not emerge. We do not consider this model here because of insufficient energetics to describe the neutrino event.

[1] S. Reusch, simeonreusch/at2019fdr: V0.2 pre-release, https://doi.org/10.5281/zenodo.5599462 (2021).
[2] Nordin, J. et al., Astron. Astrophys. 631, A147 (2019).
[3] M. Rigault, ztfquery, a python tool to access ztf data, https://doi.org/10.5281/zenodo.1345222 (2018).
[4] R. Stein, GCN Circ. 27865 (2020).
[5] A. Albert et al. (ANTARES Collaboration), Astrophys. J. 920, 50 (2021).
[6] Gaia Collaboration, Astron. Astrophys. 616, A1 (2018).
[7] S. van Velzen et al., in preparation (2021), arXiv:2111.09391 [astro-ph.HE].
[8] H. Ayala, GCN Circ. 27873 (2020).
[9] V. Savchenko, GCN Circ. 27866 (2020).
[10] R. Sunyaev et al., A&A 656, A132 (2021).
[11] Predehl, P. et al., Astron. Astrophys. 647, A1 (2021).
[12] S. Sazonov et al., Mon. Not. R. Astron. Soc. 10.1093/mnras/stab2843 (2021).
[13] N. Ben Bekhti et al. (HI4PI Collaboration), Astron. Astrophys. 594, A116 (2016).
[14] S. Frederick et al., Astrophys. J. 920, 56 (2021).
[15] U. S. S. D. Centre, Swift xrt data products generator, https://www.swift.ac.uk/user_objects (2020).
[16] P. A. Evans et al., Mon. Not. R. Astron. Soc. 397, 1177 (2009).
[17] M. Arida and E. Sabol, Heasarc webpimms, https://heasarc.gsfc.nasa.gov/cgi-bin/Tools/w3pimms/w3pimms.pl (2020).
[18] S. Reusch, ztffps v1.0.3, https://doi.org/10.5281/zenodo.5119152 (2020).
[19] M. Rigault, ztflc, https://github.com/mickaelrigault/ztflc (2020).
[20] A. A. Breeveld, W. Landsman, S. T. Holland, P. Roming, N. P. M. Kuin, and M. J. Page, in American Institute of Physics Conference Series, American Institute of Physics Conference Series, Vol. 1358, edited by J. E. McEnery, J. L. Racusin, and N. Gehrels (2011) pp. 373–376.
[21] J. C. Wilson et al., in Instrument Design and Performance for Optical/Infrared Ground-based Telescopes, Society of Photo-Optical Instrumentation Engineers (SPIE) Conference Series, Vol. 4841, edited by M. Iye and A. F. M. Moorwood (2003) pp. 451–458.
[22] K. De et al., Publ. Astron. Soc. Pac. 132, 025001 (2020).
[23] M. F. Skrutskie et al., Astron. J. 131, 1163 (2006).
[24] C. Y. Peng, L. C. Ho, C. D. Impey, and H.-W. Rix, Astron. J. 124, 266 (2002).
[25] L. Bradley et al., astropy/photutils: 1.0.0 (2020).
[26] D. G. York et al., Astrophys. J. 120, 1579 (2000).
[27] S. van Velzen, T. W. S. Holoien, F. Onori, T. Hung, and I. Arcavi, Space Sci. Rev. 216, 124 (2020).
[28] D. C. Martin et al., Astrophys. J. 619, L1 (2005).
[29] C. Million, S. W. Fleming, B. Shiao, M. Seibert, P. Loyd, M. Tucker, R. Thompson, and R. L. White, Astrophys. J. 833, 292 (2016).
[30] C. Stoughton et al., Astron. J. 123, 485 (2002).
[31] A. Lawrence et al., Mon. Not. R. Astron. Soc. 379, 1599 (2007).
[32] C. Conroy and J. E. Gunn, Astrophys. J. 712, 833 (2010).
[33] D. Foreman-Mackey, J. Sick, and B. Johnson, python-fsps: Python bindings to FSPS (v0.1.1) (2014).

[34] E. L. Wright *et al.*, Astron. J. **140**, 1868–1881 (2010).

[35] A. Mainzer *et al.*, Astrophys. J. **731**, 53 (2011).

[36] D. O. Jones, D. M. Scolnic, and S. A. Rodney, Python-Phot: Simple DAOPHOT-type photometry in Python (2015), ascl:1501.010.

[37] F. Masci, ICORE: Image Co-addition with Optional Resolution Enhancement (2013), ascl:1302.010.

[38] R. Stein *et al.*, Nature Astron. **5**, 510 (2021).

[39] M. Lacy *et al.*, Publ. Astron. Soc. Pac. **132**, 035001 (2020).

[40] R. Barniol Duran, E. Nakar, and T. Piran, Astrophys. J. **772**, 78 (2013).

[41] G. Morlino and D. Caprioli, Astron. Astrophys. **538**, A81 (2012).

[42] T. Eftekhari, E. Berger, B. A. Zauderer, R. Margutti, and K. D. Alexander, Astrophys. J. **854**, 86 (2018).

[43] A. Horesh *et al.*, Mon. Not. R. Astron. Soc. **436**, 1258 (2013).

[44] A. Generozov, P. Mimica, B. D. Metzger, N. C. Stone, D. Giannios, and M. A. Aloy, Mon. Not. R. Astron. Soc. **464**, 2481 (2017).

[45] M. Newville, T. Stensitzki, D. B. Allen, and A. Ingargiola, LMFIT: Non-Linear Least-Square Minimization and Curve-Fitting for Python (2021).

[46] B. Kyle, extinction, https://doi.org/10.5281/zenodo.804967 (2016).

[47] D. Calzetti, L. Armus, R. C. Bohlin, A. L. Kinney, J. Koornneef, and T. Storchi-Bergmann, Astrophys. J. **533**, 682 (2000).

[48] S. van Velzen, A. J. Mendez, J. H. Krolik, and V. Gorjian, Astrophys. J. **829**, 19 (2016).

[49] M. Vestergaard and B. M. Peterson, Astrophys. J. **641**, 689 (2006).

[50] H. Guo, Y. Shen, and S. Wang, PyQSOFit: Python code to fit the spectrum of quasars (2018), ascl:1809.008.

[51] E. L. Fitzpatrick, Publications of the ASP **111**, 63 (1999).

[52] D. J. Schlegel, D. P. Finkbeiner, and M. Davis, Astrophys. J. **500**, 525 (1998).

[53] T. A. Boroson and R. F. Green, Astrophys. J. Suppl. Ser. **80**, 109 (1992).

[54] Y. Shen *et al.*, Astrophys. J. Suppl. Ser. **194**, 45 (2011).

[55] H. Guo, X. Liu, Y. Shen, A. Loeb, T. Monroe, and J. X. Prochaska, Mon. Not. R. Astron. Soc. **482**, 3288 (2019).

[56] Y. Shen *et al.*, Astrophys. J., Suppl. Ser. **241**, 34 (2019).

[57] R. J. McLure and J. S. Dunlop, Mon. Not. R. Astron. Soc. **331**, 795 (2002).

[58] M. T. Patterson *et al.*, Publ. Astron. Soc. Pac. **131**, 018001 (2018).

[59] F. J. Masci *et al.*, Publ. Astron. Soc. Pac. **131**, 018003 (2018).

[60] S. van Velzen *et al.*, Astrophys. J. **908**, 4 (2021).

[61] E. Blaufuss, GCN Circ. **24378** (2019).

[62] R. Stein, A. Franckowiak, J. van Santen, L. Rauch, M. M. Kasliwal, I. Andreoni, T. Ahumada, M. Coughlin, L. P. Singer, and S. Anand, The Astronomer's Telegram **12730**, 1 (2019).

[63] E. Blaufuss, GCN Circ. **24910** (2019).

[64] R. Stein *et al.*, The Astronomer's Telegram **12879**, 1 (2019).

[65] R. Stein, GCN Circ. **25225** (2019).

[66] R. Stein, A. Franckowiak, M. M. Kasliwal, I. Andreoni, M. Coughlin, L. P. Singer, F. Masci, and S. van Velzen, The Astronomer's Telegram **12974**, 1 (2019).

[67] E. Blaufuss, GCN Circ. **25806** (2019).

[68] R. Stein, A. Franckowiak, M. Kowalski, and M. Kasliwal, The Astronomer's Telegram **13125**, 1 (2019).

[69] R. Stein, A. Franckowiak, M. Kowalski, and M. Kasliwal, GCN Circ. **25824** (2019).

[70] R. Stein, GCN Circ. **25913** (2019).

[71] R. Stein, A. Franckowiak, J. Necker, S. Gezari, and S. v. Velzen, The Astronomer's Telegram **13160**, 1 (2019).

[72] R. Stein, A. Franckowiak, J. Necker, S. Gezari, and S. van Velzen, GCN Circ. **25929** (2019).

[73] R. Stein, GCN Circ. **26655** (2020).

[74] R. Stein and S. Reusch, GCN Circ. **26667** (2020).

[75] R. Stein, GCN Circ. **26696** (2020).

[76] S. Reusch and R. Stein, GCN Circ. **26747** (2020).

[77] C. Lagunas Gualda, GCN Circ. **26802** (2020).

[78] S. Reusch and R. Stein, GCN Circ. **26813** (2020).

[79] S. Reusch and R. Stein, GCN Circ. **26816** (2020).

[80] C. Lagunas Gualda, GCN Circ. **27719** (2020).

[81] S. Reusch, R. Stein, and A. Franckowiak, GCN Circ. **27721** (2020).

[82] R. Stein, GCN Circ. **27865** (2020).

[83] S. Reusch, R. Stein, A. Franckowiak, and S. Gezari, GCN Circ. **27872** (2020).

[84] S. Reusch, R. Stein, A. Franckowiak, J. Sollerman, T. Schweyer, and C. Barbarino, GCN Circ. **27910** (2020).

[85] S. Reusch, R. Stein, A. Franckowiak, J. Necker, J. Sollerman, C. Barbarino, and T. Schweyer, GCN Circ. **27980** (2020).

[86] M. Santander, GCN Circ. **27997** (2020).

[87] S. Reusch, R. Stein, and A. Franckowiak, GCN Circ. **28005** (2020).

[88] E. Blaufuss, GCN Circ. **28433** (2020).

[89] S. Reusch, R. Stein, A. Franckowiak, I. Andreoni, and M. Coughlin, GCN Circ. **28441** (2020).

[90] S. Reusch, R. Stein, A. Franckowiak, S. Schulze, and J. Sollerman, GCN Circ. **28465** (2020).

[91] C. Lagunas Gualda, GCN Circ. **28504** (2020).

[92] S. Reusch, R. Stein, S. Weimann, and A. Franckowiak, GCN Circ. **28520** (2020).

[93] C. Lagunas Gualda, GCN Circ. **28532** (2020).

[94] S. Weimann, R. Stein, S. Reusch, and A. Franckowiak, GCN Circ. **28551** (2020).

[95] M. Santander, GCN Circ. **28575** (2020).

[96] S. Reusch, S. Weimann, R. Stein, and A. Franckowiak, GCN Circ. **28609** (2020).

[97] C. Lagunas Gualda, GCN Circ. **28715** (2020).

[98] R. Stein, S. Reusch, S. Weimann, and M. Coughlin, GCN Circ. **28757**, 1 (2020).

[99] C. Lagunas Gualda, GCN Circ. **28969** (2020).

[100] S. Weimann, R. Stein, S. Reusch, and A. Franckowiak, GCN Circ. **28989**, 1 (2020).

[101] C. Lagunas Gualda, GCN Circ. **29012** (2020).

[102] S. Reusch, S. Weimann, R. Stein, and A. Franckowiak, GCN Circ. **29031** (2020).

[103] E. Blaufuss, GCN Circ. **29120** (2020).

[104] R. Stein, S. Weimann, S. Reusch, and A. Franckowiak, GCN Circ. **29172** (2020).

[105] C. Lagunas Gualda, GCN Circ. **29454** (2021).

[106] S. Reusch, S. Weimann, R. Stein, M. Coughlin, and A. Franckowiak, GCN Circ. **29461** (2021).

[107] M. Santander, GCN Circ. **29976** (2021).

[108] R. Stein, S. Weimann, J. Necker, S. Reusch, and A. Franckowiak, GCN Circ. **29999** (2021).

[109] M. Santander, GCN Circ. **30342** (2021).
[110] J. Necker, R. Stein, S. Weimann, S. Reusch, and A. Franckowiak, GCN Circ. **30349** (2021).
[111] M. Santander, GCN Circ. **30627** (2021).
[112] R. Stein, S. Weimann, S. Reusch, J. Necker, A. Franckowiak, and M. Coughlin, GCN Circ. **30644** (2021).
[113] M. Lincetto, GCN Circ. **30862** (2021).
[114] S. Weimann, S. Reusch, J. Necker, R. Stein, and A. Franckowiak, GCN Circ. **30870** (2021).
[115] K. Murase, S. S. Kimura, B. T. Zhang, F. Oikonomou, and M. Petropoulou, Astrophys. J. **902**, 108 (2020).
[116] K. Hayasaki and R. Yamazaki, Astrophys. J. **886**, 114 (2019).
[117] K. Murase, S. S. Kimura, and P. Mészáros, Phys. Rev. Lett. **125**, 011101 (2020).
[118] S. S. Kimura, K. Murase, and K. Toma, Astrophys. J. **806**, 159 (2015).
[119] J. C. McKinney, L. Dai, and M. J. Avara, Mon. Not. R. Astron. Soc. **454**, L6 (2015).
[120] Y.-F. Jiang, J. M. Stone, and S. W. Davis, Astrophys. J. **880**, 67 (2019).
[121] E. Takeo, K. Inayoshi, K. Ohsuga, H. R. Takahashi, and S. Mineshige, Mon. Not. R. Astron. Soc. **488**, 2689 (2019).
[122] A. Mücke, R. Engel, J. P. Rachen, R. J. Protheroe, and T. Stanev, Computer Phys. Comm. **124**, 290 (2000).
[123] Y. Io and T. K. Suzuki, Astrophys. J. **780**, 46 (2014).
[124] Y.-F. Jiang, J. M. Stone, and S. W. Davis, Astrophys. J. **784**, 169 (2014).
[125] H. R. Takahashi, K. Ohsuga, T. Kawashima, and Y. Sekiguchi, Astrophys. J. **826**, 23 (2016).
[126] L. E. Strubbe and E. Quataert, Mon. Not. R. Astron. Soc. **400**, 2070 (2009).
[127] M. C. Miller, Astrophys. J. **805**, 83 (2015).
[128] B. D. Metzger and N. C. Stone, Mon. Not. R. Astron. Soc. **461**, 948 (2016).
[129] W. Winter and C. Lunardini, Nature Astron. **5**, 472 (2021).
[130] L. Dai, J. C. McKinney, N. Roth, E. Ramirez-Ruiz, and M. C. Miller, Astrophys. J. **859**, L20 (2018).
[131] A. Mummery and S. A. Balbus, Mon. Not. R. Astron. Soc. **504**, 4730 (2021).
[132] A. Mummery, Mon. Not. R. Astron. Soc., submitted (2021), arXiv:2104.06212 [astro-ph.HE].
[133] A. Mummery, Mon. Not. R. Astron. Soc. **504**, 5144 (2021).
[134] A. Mummery and S. A. Balbus, Mon. Not. R. Astron. Soc. **505**, 1629 (2021).
[135] C. S. Kochanek, Mon. Not. R. Astron. Soc. **461**, 371 (2016).
[136] M. J. Rees, Nature **333**, 523 (1988).
[137] F. De Colle, J. Guillochon, J. Naiman, and E. Ramirez-Ruiz, Astrophys. J. **760**, 103 (2012).
[138] K. Murase, Y. Inoue, and C. D. Dermer, Phys. Rev. D **90**, 023007 (2014).
[139] P. Mohan, T. An, Y. Zhang, J. Yang, X. Yang, and A. Wang, arXiv e-prints , arXiv:2106.15799 (2021), arXiv:2106.15799 [astro-ph.HE].
[140] T. Matsumoto, T. Piran, and J. H. Krolik, Mon. Not. R. Astron. Soc. 10.1093/mnras/stac382 (2022).